nature geoscience

ARTICLES

https://doi.org/10.1038/s41561-021-00735-y

Microbial methylation potential of mercury sulfide particles dictated by surface structure

Li Tian[1], Wenyu Guan[1], Yunyun Ji[1], Xin He[1], Wei Chen[1], Pedro J. J. Alvarez[2] and Tong Zhang[1]✉

Environmental contamination by mercury in its organometallic form, methylmercury, remains a major global concern due to its neurotoxicity, environmental persistence and biomagnification through the food chain. Accurate prediction of mercury methylation cannot be achieved based on aqueous speciation alone, and there remains limited mechanistic understanding of microbial methylation of particulate-phase mercury. Here we assess the time-dependent changes in structural properties and methylation potential of nanoparticulate mercury using microscopic and spectroscopic analyses, microcosm bioassays and theoretical calculations. We show that the methylation potential of a mercury sulfide mineral ubiquitous in contaminated soils and sediments (nanoparticulate metacinnabar) is determined by its crystal structure. Methylmercury production increases when more of nano-metacinnabar's exposed surfaces occur as the (111) facet, due to its large binding affinity to methylating bacteria, likely via the protein transporter responsible for mercury cellular uptake prior to methylation. During nanocrystal growth, the (111) facet diminishes, lessening methylation of nano-metacinnabar. However, natural ligands alleviate this process by preferentially adsorbing to the (111) facet, and consequently hinder natural attenuation of mercury methylation. We show that the methylation potential of nanoparticulate mercury is independent of surface area. Instead, the nano-scale surface structure of nanoparticulate mercury is crucial for understanding the environmental behaviour of mercury and other nutrient or toxic soft elements.

Methylmercury (MeHg) production is primarily mediated by anaerobic microorganisms in natural aquatic environments[1] and largely determined by the bioavailability of inorganic mercury to microbial methylators[2]. A variety of mercury species, including elemental mercury[3,4], dissolved mercury complexes[5] and mercury sulfide (HgS) nanoparticles[6], have been demonstrated to be available for methylation. In recent years, a growing body of evidence has revealed that MeHg production cannot be accurately predicted by the aqueous speciation of mercury alone, pointing to the essential role of particulate phases in controlling mercury methylation[7–10]. In fact, nanoparticulate mercury has been detected in various environmental matrices, such as soils, marshes and estuarine and marine water and sediments, which are natural 'hotspots' of MeHg production and accumulation[11–15]. Due to the kinetically hindered mineralization processes in the presence of the ubiquitous natural organic matter (NOM) and sulfide[16–18], mercury-containing nanoparticles are expected to be prevalent in anaerobic environments. Moreover, with the recently proposed biological and photochemical pathways for the formation of mercury sulfide nanoparticles, the known occurrence of nanoparticulate mercury has extended to 'new' natural settings (for example, non-sulfidic condition, oxygenated environment)[19–22]. Hence, elucidating the mechanisms of and factors affecting the microbial methylation potential of mercury sulfide nanoparticles is critical for establishing risk assessment models of mercury pollution and understanding global biogeochemical cycling of mercury.

It is well known that nanoparticles are widely present in all environmental compartments due to natural and anthropogenic processes, and that they often exhibit environmental behaviours that are different from their bulk-scale counterparts because of the unique physicochemical properties at the nano-scale[23–26]. Indeed, nanoparticulate metacinnabar (a crystalline phase of HgS) appears to be significantly more available for microbial methylation compared with bulk-scale metacinnabar[6,8]; however, the methylation potential of this nanoparticulate mercury phase drastically decreases during ageing[6]. Here, we demonstrate that the ageing-induced changes in the bioavailability of nanoparticulate mercury for methylation are independent of the surface area or size of the nanoparticles; rather, it is dictated by the exposed facet, an intrinsic property of crystalline nanoparticles that defines nano-specific interfacial reactions.

Surface-area-independent decrease of nano-HgS methylation

Mercury sulfide nanoparticles remained bioavailable for methylation during the entire ageing period in this research (0–21 days), and the methylation potential of nanoparticulate mercury was altered by ageing in a manner independent of surface area (Fig. 1). Ionic mercury and sulfide were precipitated in the presence of naturally occurring ligands that often co-exist with mercury in environmental matrices, including Suwannee River humic acid (SRHA), Suwannee River fulvic acid (SRFA) and glutathione (GSH), and the precipitation products were immediately formed and allowed to age in anaerobic water for up to 21 days. The dominant products were nanoparticulate metacinnabar with particle diameter of 4.8–7.4 nm. These nanoparticles were relatively stable in size, surface area and aggregation status during ageing (Fig. 1e,f, Supplementary Figs. 1–3 and Supplementary Table 1), which corroborates previous studies that demonstrated the persistence of nanoparticulate mercury in aquatic environments[11–16,18,27].

After ageing for different time periods, the HgS nanoparticles were exposed to sulfate reducing bacteria (that is, *Desulfovibrio desulfuricans* ND132), a major microbial group that drives mercury methylation in the environment[1,28]. The total mercury addition and microbial growth were consistent among all treatments receiving

[1]College of Environmental Science and Engineering, Ministry of Education Key Laboratory of Pollution Processes and Environmental Criteria, Tianjin Key Laboratory of Environmental Remediation and Pollution Control, Nankai University, Tianjin, China. [2]Department of Civil and Environmental Engineering, Rice University, Houston, TX, USA. ✉e-mail: zhangtong@nankai.edu.cn

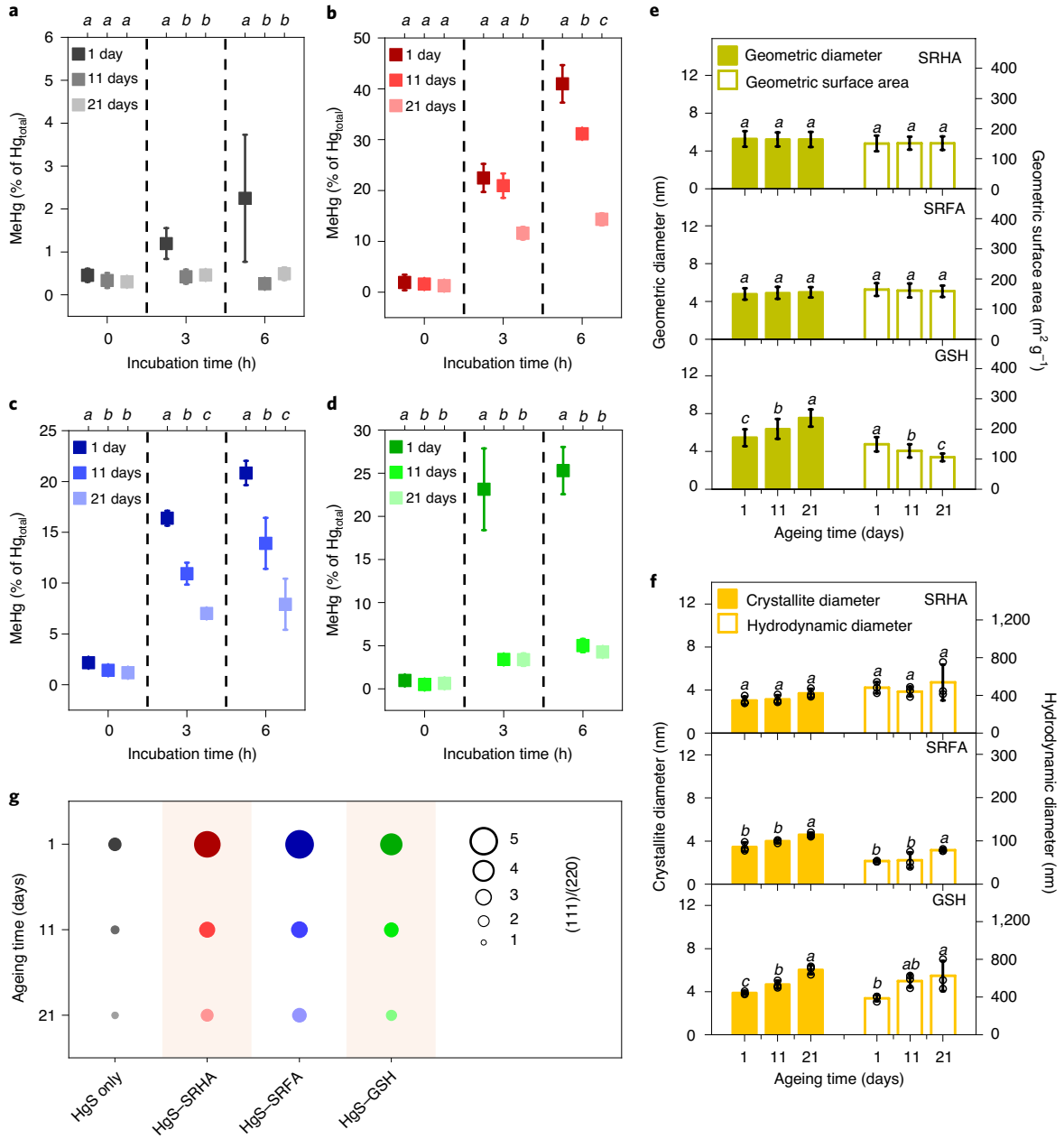

Fig. 1 | Methylation potential and exposed facets of nano-HgS significantly change during ageing while particle size and surface area remain similar. **a**–**d**, MeHg production by *D. desulfuricans* ND132 normalized to the total mercury concentrations after exposure to 10 nM HgS formed in the absence of natural ligands (**a**) and nano-HgS co-precipitated with SRHA (**b**), SRFA (**c**) or GSH (**d**), and aged for 1, 11 or 21 days. Values that are statistically different ($P < 0.05$) among treatments with different ageing time according to one-way ANOVA are indicated by italic lowercase letters. Error bars represent ±1 standard deviation (s.d.) of replicate bacterial cultures ($n = 3$). **e**, Geometric diameter and geometric surface area of nano-HgS co-precipitated with natural ligands and aged for different time periods. Values that are statistically different ($P < 0.05$) among treatments with different ageing time according to one-way ANOVA are indicated by italic lowercase letters. Error bars represent ±1 s.d. of nanoparticles observed by TEM ($n = 100$). **f**, Crystallite diameter and hydrodynamic diameter of nano-HgS co-precipitated with natural ligands and aged for different time periods. Crystallite diameters were calculated according to the Scherrer formula[60] using the XRD data (Supplementary Fig. 6). Values that are statistically different ($P < 0.05$) among treatments with different ageing time according to one-way ANOVA are indicated by italic lowercase letters. Error bars represent ±1 s.d. of replicate nanoparticle samples ($n = 3$). **g**, Relative content of metacinnabar (111) facet in HgS formed in the presence or absence of natural ligands.

HgS aged for different time periods (Supplementary Figs. 4 and 5). The control group of HgS that precipitated without ligands exhibited minimal methylation potential (Fig. 1a). MeHg production from HgS nanoparticles formed in the presence of natural ligands diminished with ageing time (Fig. 1b–d), which cannot be explained by the ageing-induced changes in the geometric diameter, surface area, crystallite diameter, hydrodynamic diameter or zeta potential of the nanoparticles (Fig. 1e,f and Supplementary Table 1). For instance, during ageing from 1 to 21 days, the methylation potential of SRHA–HgS and SRFA–HgS nanoparticles (that is, nanoparticles

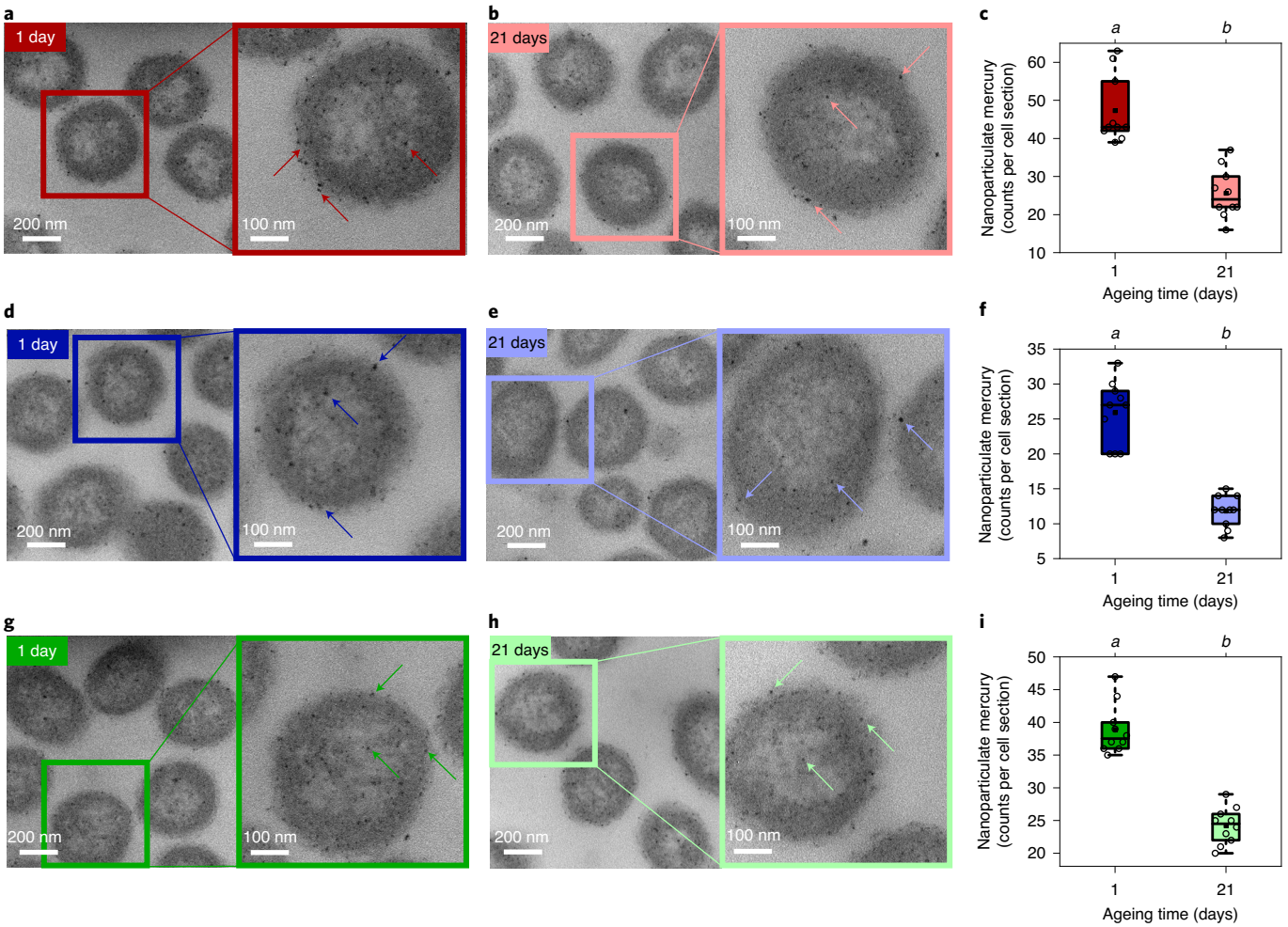

Fig. 2 | Association between methylating bacterial cells and nano-HgS significantly decreases during ageing. a,**b**,**d**,**e**,**g**,**h**, TEM images of *D. desulfuricans* ND132 after exposure to nano-HgS co-precipitated with SRHA (**a**,**b**), SRFA (**d**,**e**) or GSH (**g**,**h**) and aged for 1 day (**a**,**d**,**g**) or 21 days (**b**,**e**,**h**). The arrows point to nanoparticulate mercury associated with methylating bacterial cells. **c**,**f**,**i**, Nanoparticulate mercury counts per cell section of *D. desulfuricans* ND132 (open circles) after exposure to nano-HgS co-precipitated with SRHA (**c**), SRFA (**f**) or GSH (**i**). The bottom and top of the boxes show the first and third quartiles, respectively, the bar in the middle shows the median, the black solid dot shows the average value and the whiskers show the minimum and maximum values of replicate cell sections ($n = 10$). Values that are statistically different ($P < 0.05$) between treatments with different ageing time according to the two-tailed independent *t* test are indicated by italic lowercase letters.

formed from precipitation of HgS in the presence of SRHA or SRFA) decreased by 65.0% and 62.0%, respectively (Fig. 1b,c), whereas the changes in the size, surface area and charge of these particles were statistically insignificant (Fig. 1e,f and Supplementary Table 1). In general, nanoparticles tend to be highly reactive because of their large specific surface area[23–26]. However, in the case of microbial methylation of nanoparticulate mercury, structural surface properties other than surface area determined the reactivity of these nanoparticles.

Facet-dependent methylation potential of nano-HgS

The exposed crystal facets of nanoparticulate metacinnabar changed during ageing and strongly influenced the bioavailability and methylation potential of HgS nanoparticles (Fig. 1 and Supplementary Figs. 4–6). The dominant exposed facet of HgS (precipitated with or without natural ligands) was the (111) facet of metacinnabar according to the corresponding characteristic peak in the X-ray diffraction (XRD) spectra (Supplementary Fig. 6) and the lattice spacing in high-resolution transmission electron microscopy (HR-TEM) images (Supplementary Figs. 1–3). The relative intensity of the (111) peak versus (220) peak in the XRD spectra was used to estimate the relative content of these facets[29]. The relative content of the (111) facet of metacinnabar generally decreased during ageing (Fig. 1g), indicating fast crystal growth along this dominant facet[30]. More importantly, this trend of changing exposed facets coincides with that of reducing methylation potential of HgS during ageing (Fig. 1a–d), which underscores the potential role of the (111) facet in supplying bioavailable mercury for methylation. When mercury sulfide was co-precipitated with natural ligands, SRHA, SRFA and GSH, a markedly larger content of metacinnabar (111) facet was detected from the precipitation products (that is, HgS nanoparticles), particularly during the early stage of mineralization (0–1 days), in comparison with the HgS precipitated without ligands (Fig. 1g). These results may, at least partially, explain the enhancing effect of NOM and low-molecular-weight (LMW) thiol ligands on mercury methylation reported in previous field and laboratory investigations[9,31,32].

To further discern the role of exposed facet in modulating microbial methylation of nanoparticulate mercury, two model metacinnabar materials with relatively high (111) content (model material I)

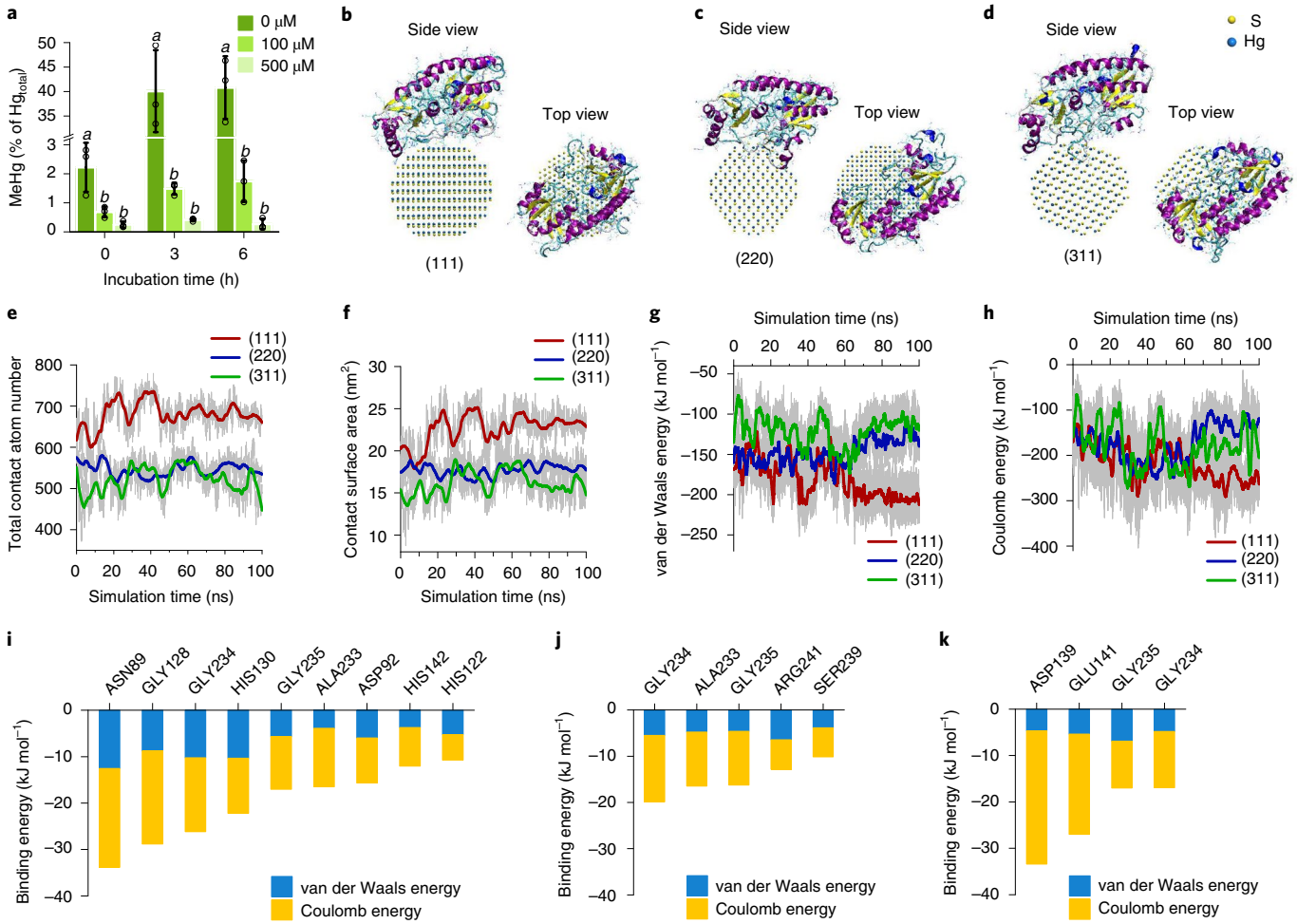

Fig. 3 | (111) facet of nano-metacinnabar exhibits higher affinity for the divalent metal transporter of *D. desulfuricans* ND132 than the other facets. **a**, MeHg production by *D. desulfuricans* ND132 normalized to the total mercury concentrations after exposure to Zn(II) and 10 nM nano-HgS co-precipitated with GSH and aged for 1 day. Values that are statistically different ($P < 0.05$) among treatments with different concentrations of Zn(II) according to one-way ANOVA are indicated by italic lowercase letters. Error bars represent ±1 s.d. of replicate bacterial cultures ($n = 3$). **b**–**d**, Binding conformation of periplasmic solute-binding protein of zinc transport system of *D. desulfuricans* ND132, ZnuA, on facets (111) (**b**), (220) (**c**) and (311) (**d**) at 100 ns of MD simulations. **e**, Time-dependent total contact atom number of an individual ZnuA within 1 nm from different facets of nano-metacinnabar during MD simulations. **f**, Time-dependent contact surface area of an individual ZnuA on different facets of metacinnabar during MD simulations. **g**,**h**, Time-dependent van der Waals energy (**g**) and Coulomb energy (**h**) of ZnuA on different facets of metacinnabar during MD simulations. **i**–**k**, Binding energy of key amino acid residues (binding energy < –10 kJ mol^{-1}) associated with facets (111) (**i**), (220) (**j**) and (311) (**k**) within 1 nm at the last 5 ns of MD simulations.

and low (111) content (model material II) were synthesized and examined in microbial methylation experiments (Supplementary Figs. 7 and 8 and Supplementary Table 2). These model materials were nano-scale particles that exhibited similar size and morphology (Supplementary Fig. 7 and Supplementary Table 2). After incubation with the methylating bacteria *D. desulfuricans* ND132, MeHg production from material I was significantly greater than from material II, while the total mercury concentrations and cell numbers were rather similar in all test cultures (Supplementary Fig. 8). Taken together, our results reveal that nano-scale metacinnabar (that occurs during the early mercury mineralization stage) likely represents the bioavailable particulate-phase precursor for MeHg production, and exposed facet is a crucial parameter for determining the methylation potential of nano-metacinnabar.

Facet-dependent bacterial association of nano-HgS

Our previous research on microbial methylation of HgS nanoparticles presumed the potential correlation between MeHg production and the release of dissolved mercury species (<20 nm) from particulate phase, which explained the variation in the bioavailability of nanoparticulate versus bulk-particulate mercury[6]. Nevertheless, recent mercury methylation studies showed that the bioavailability of particulate mercury cannot be accurately assessed by the leaching potential of inorganic mercury species into bulk solution[8,33]. In fact, bacteria–mineral association has been shown to be important for bio-transformation of goethite nanoparticles[34], and inorganic mercury appeared to be strongly associated with bacterial cells through thiol-containing ligands[3,35,36], which apparently influenced the subsequent cellular uptake and methylation of mercury[10,37,38]. In this study, ageing remarkably decreased the binding affinity and subsequent availability of nano-HgS to methylating bacteria, likely by altering the exposed facets of metacinnabar nanoparticles (Figs. 2 and 3).

We first conducted transmission electron microscopy coupled with energy-dispersive spectroscopy (TEM-EDX) analysis of thin sections of *D. desulfuricans* ND132 after nano-HgS exposure, and

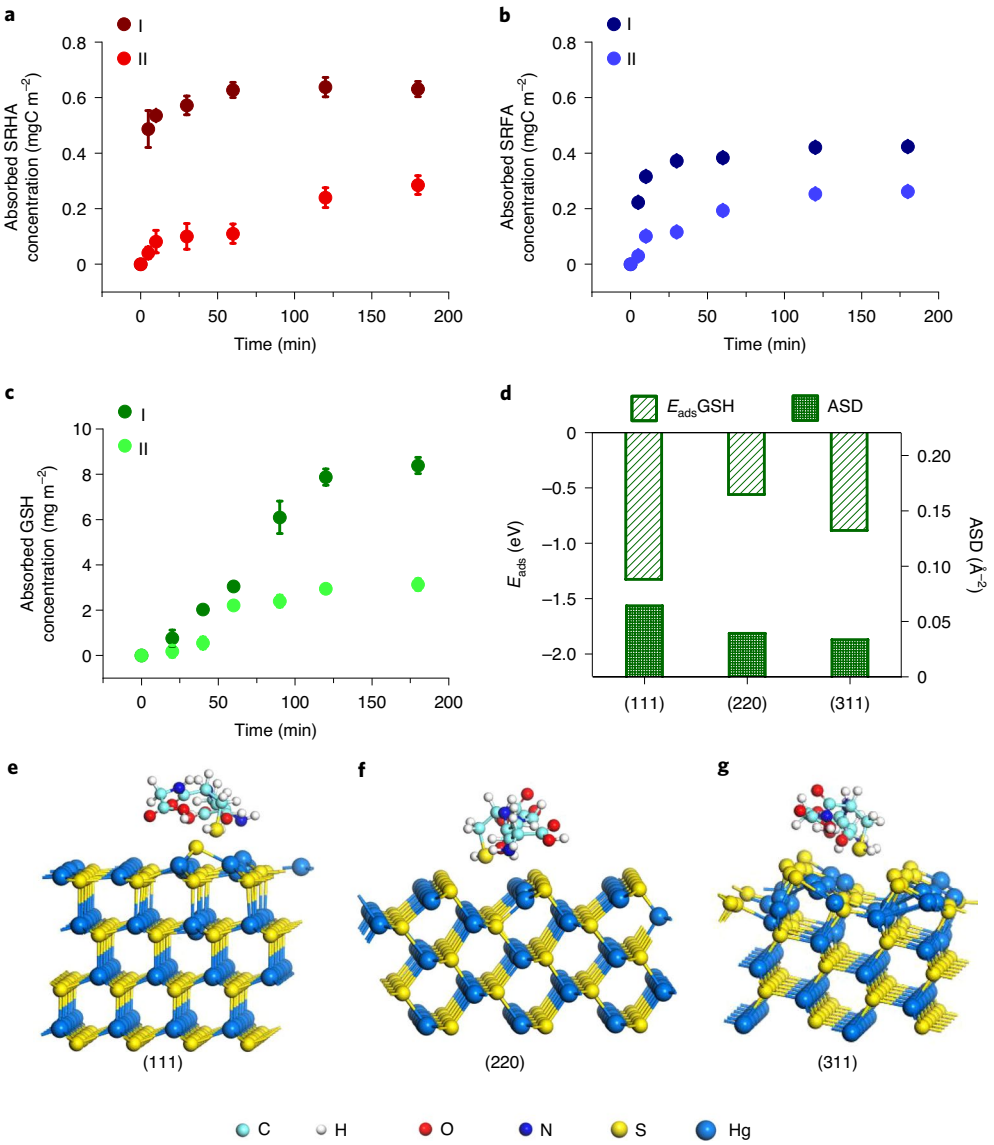

Fig. 4 | (111) facet of nano-metacinnabar preferentially adsorbs natural ligands. a–c, Adsorption of SRHA (**a**), SRFA (**b**) and GSH (**c**) to model nano-HgS I versus II. Error bars represent ±1 s.d. of replicate nanoparticle samples ($n = 3$). **d**, Adsorption energy (E_{ads}) and active site density (ASD) of different crystal facets of metacinnabar adsorbed with GSH according to DFT calculations. **e–g**, Three-dimensional views of GSH molecules adsorbed to facets (111) (**e**), (220) (**f**) and (311) (**g**) of metacinnabar.

observed that metacinnabar nanoparticles formed with natural ligands and aged for different time periods were all abundantly associated with bacterial cells (Fig. 2 and Supplementary Fig. 9). The TEM images illustrated that nano-HgS attached to the inner and outer membranes as well as penetrated into the periplasm and cytosol, with the total number of cell-associated nanoparticles substantially decreasing upon ageing from 1 to 21 days (Fig. 2 and Supplementary Fig. 9). Facet-engineered model materials were used to connect this ageing-reduced cell association with ageing-induced changes of exposed facets of metacinnabar. After separating the cell-bound nanoparticles from the freely suspended nanoparticles using density gradient centrifugation, the extent of nanoparticle–cell binding was quantified and appeared to be significantly larger for model material I than for model material II (Supplementary Fig. 8b). These data suggest that nanoparticle–cell association is facet dependent and that the (111) facet of metacinnabar has the highest affinity to the methylating bacteria.

Multiple lines of evidence have pointed to the essential role of periplasmic divalent metal transporters in dictating cellular transport of inorganic mercury across the bacterial cell membrane before intracellular methylation[38–43]. Here we show that, upon exposure to the same amount of inorganic mercury (Supplementary Fig. 10), addition of divalent zinc, Zn(II), to cultures of *D. desulfuricans* ND132 considerably inhibited microbial methylation of nano-HgS (Fig. 3a). This suggests the validity of using the zinc transport system of *D. desulfuricans* ND132 to investigate the facet-dependent binding and intracellular transport of nanoparticulate metacinnabar. Thus, binding of different exposed facets of nanoparticulate metacinnabar with a periplasmic substrate-binding protein of the zinc transport system of *D. desulfuricans* ND132, ZnuA[44], was assessed using molecular dynamics (MD) simulations (Fig. 3b–k). Compared with the (220) and (311) facets, the (111) facet associated more sufficiently with ZnuA, as indicated by the larger facet–protein contact atom number and contact surface area (Fig. 3b–f).

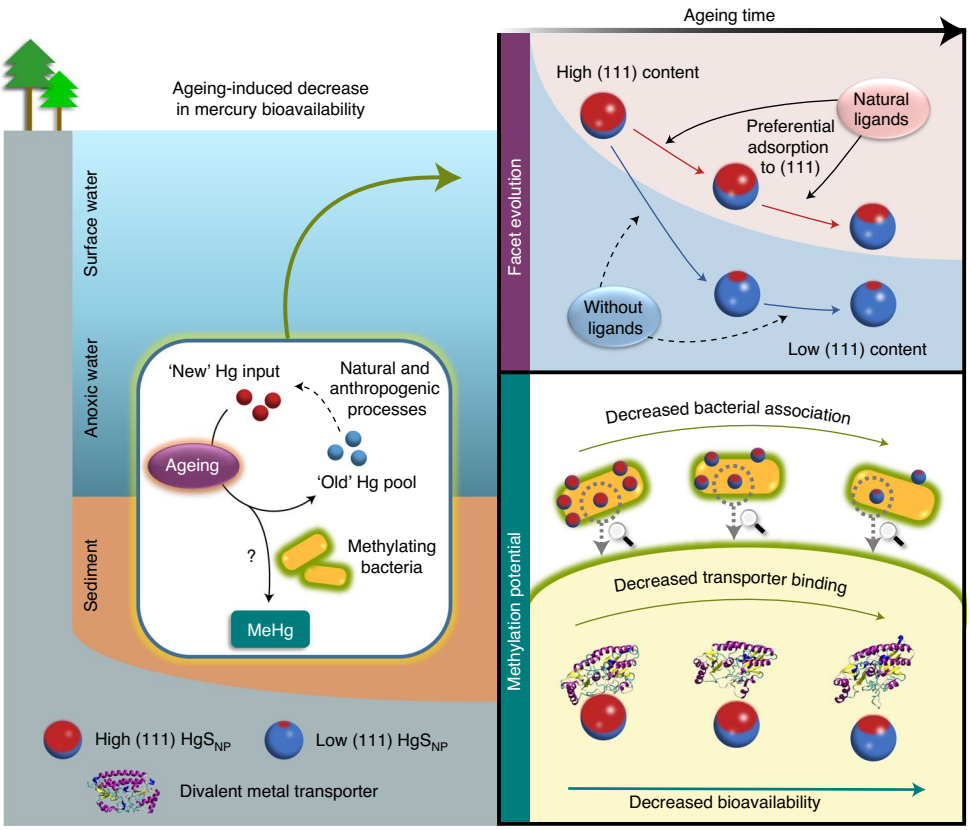

Fig. 5 | Conceptual illustration of ageing-induced decrease in bioavailability and methylation potential of nano-metacinnabar due to facet evolution. The (111) facet of nano-metacinnabar diminishes during ageing, and this process is mitigated by the preferential adsorption of natural ligands onto (111) facet, relative to the other exposed facets of metacinnabar. Nano-metacinnabar with large content of (111) facet strongly associates with divalent metal transporters of methylating bacteria, which may enhance cellular uptake and methylation of nanoparticulate mercury. These findings explain the greater MeHg production from the 'new' mercury input compared with the 'old' environmental mercury pool, which may be 'renewed' by various natural and anthropogenic processes. 'HgS_{NP}' refers to HgS nanoparticles.

Within 1 nm interfacial distance, a variety of amino acid residues, including asparagine (ASN), glycine (GLY), histidine (HIS), alanine (ALA) and aspartic acid (ASP), strongly bound to the (111) facet (Fig. 3i), whereas fewer strong binding sites of ZnuA (with binding energy < -10 kJ mol^{-1}) were detected on the (220) facet (Fig. 3j) and the (311) facet (Fig. 3k). The amino acid residues that appeared to interact with all three exposed facets, such as GLY234, displayed evidently stronger binding to the (111) facet than to the other facets (Fig. 3i–k). Both van der Waals force and electrostatic interaction (measured via the van der Waals energy and Coulomb energy of the facet–protein systems) contributed to this facet-dependent transporter binding (Fig. 3g–k). The favoured binding of metacinnabar (111) facet with metal transporters likely facilitates uptake and methylation of mercury, which makes this facet relatively more bioavailable.

Facet-dependent preferential adsorption of natural ligands

The (111) facet of metacinnabar that actively participated in microbial methylation was preserved during mineralization, due to its preferential adsorption of natural ligands (Fig. 4). It is worth noting that fast crystal growth along a certain direction often results in shrinking or elimination of the corresponding facet, but this can be alleviated by adsorption of surface modifiers on the specific facets to reduce the surface energy[30,45,46]. During the early stage of HgS mineralization, three main facets, that is, (111), (220) and (311), of metacinnabar were formed immediately, and the (111) facet exhibited preferential adsorption of natural ligands, according to the experimental data of ligand adsorption onto facet-engineered model materials complemented with theoretical calculations using density functional theory (DFT) (Fig. 4). The amount of SRHA, SRFA and GSH adsorbed on model material I was consistently greater than that adsorbed on model material II, and the difference reached two- to threefold at the end of the adsorption experiments (Fig. 4a–c).

The favourable adsorption process on the (111) facet was consistent with the lower adsorption energy and larger density of active binding sites of the (111) facet toward GSH, compared with the (220) and (311) facets (Fig. 4d–g). In particular, all mercury on the (111) facet is in the form of unsaturated three-coordinated atoms, which are prone to forming inner-sphere coordination bonds and inducing chemical adsorption of ligand-rich compounds (as indicated by the apparently negative adsorption energy, −1.33 eV). Indeed, both Hg $4f_{7/2}$ and Hg $4f_{5/2}$ peaks in the X-ray photoelectron spectroscopy (XPS) spectra of nano-HgS that formed with natural ligands prominently shifted to lower binding energy values relative to the standard XPS spectrum of metacinnabar (Supplementary Fig. 11). These data confirm that the natural ligands strongly interacted with surface mercury atoms of nanoparticulate metacinnabar via inner-sphere coordination. This chemical binding remained relatively stable during ageing, as the binding energies of the mercury peaks were consistent among nano-HgS samples aged for 1, 11 and 21 days (Supplementary Fig. 11).

The facet-dependent ligand adsorption not only explains the 'protecting effect' of natural ligands on the (111) facet of metacinnabar during HgS mineralization (Fig. 1g), but is also in line with the role of ligand-rich molecules (for example, protein, peptide, surfactant and NOM) in modulating the crystalline faces of a diverse variety of pathological, engineered and naturally occurring minerals[30,45,47,48].

Implications for metal biogeochemistry

Even though the 'new' mercury input may only represent a small mercury fraction from a mass balance standpoint, it is the predominant source of MeHg that causes the environmental risks. Moreover, the vast majority of legacy mercury is susceptible to local- and global-scale perturbations, and can be 'renewed' by natural or anthropogenic processes (Fig. 5), such as global climate change, site remediation and altered landscape utilization[49–51]. In previous field studies, the methylation potential of the 'newly' deposited mercury appeared to be 1.5–2.8 times greater than that of the native mercury pool[52,53]. A similar magnitude of the ageing-induced decreases in methylation potential was observed in our research on nanoparticulate mercury; that is, newly formed nano-HgS was 1.6–4.9 times more available for microbial methylation than the nano-HgS aged during a 21-day time period, even though metacinnabar persistently remained at the nano-scale. Considering that nanoparticulate mercury accounts for a major fraction (12–93%) of the total mercury pool in natural aquatic systems[14,15], our research offers a mechanistic understanding of the dynamic changes in the methylation potential of the 'new' mercury inputs, and paves the way toward incorporating particulate phases and interfacial processes into predictive models of MeHg production (Fig. 5). This knowledge is needed to assess the time scales of biogeochemical processes leading to MeHg accumulation and subsequently informing remedial practice and management of mercury-impacted ecosystems with response time.

Preferential binding between ligand-rich molecules with fast-formed crystal faces may be Nature's tool for tailoring the crystal structure and tuning the bioavailability of reactive mineral phases. The ligand-modulated facet evolution of nanoparticles during mineralization should not be limited to mercury sulfide and could be extended to the prevalent occurrence of nanominerals containing nutrient (for example, Fe, Mn, Zn and Cu) or toxic elements (for example, Cd and Pb). These nanominerals likely represent the particulate phase that remains bioavailable for a vastly variable time period and plays vital roles in the biogeochemical cycling of the corresponding elements, leading to beneficial or detrimental environmental consequences. Hence, it is of utmost environmental significance to identify bioavailable mineral surfaces and understand structure–activity relationships influencing bioavailability. Such interactions at mineral surfaces are particularly relevant for shaping the microbial ecology of mineral-dwelling communities[54,55] that substantially contribute to the Earth's energy and biomass production (for example, chemosynthesis driven by metal sulfides[56] and extracellular electron transfer driven by metal oxides[57,58]), as well as the biogeochemical cycles of essential elements (for example, C and N)[59].

Online content

Any methods, additional references, Nature Research reporting summaries, source data, extended data, supplementary information, acknowledgements, peer review information; details of author contributions and competing interests; and statements of data and code availability are available at https://doi.org/10.1038/s41561-021-00735-y.

Received: 22 January 2020; Accepted: 12 March 2021;
Published online: 26 April 2021

References

1. Parks, J. M. et al. The genetic basis for bacterial mercury methylation. *Science* **339**, 1332–1335 (2013).
2. Hsu-Kim, H., Kucharzyk, K. H., Zhang, T. & Deshusses, M. A. Mechanisms regulating mercury bioavailability for methylating microorganisms in the aquatic environment: a critical review. *Environ. Sci. Technol.* **47**, 2441–2456 (2013).
3. Colombo, M. J., Ha, J. Y., Reinfelder, J. R., Barkay, T. & Yee, N. Anaerobic oxidation of Hg(0) and methylmercury formation by *Desulfovibrio desulfuricans* ND132. *Geochim. Cosmochim. Acta* **112**, 166–177 (2013).
4. Hu, H. Y. et al. Oxidation and methylation of dissolved elemental mercury by anaerobic bacteria. *Nat. Geosci.* **6**, 751–754 (2013).
5. Benoit, J. M., Gilmour, C. C., Mason, R. P. & Heyes, A. Sulfide controls on mercury speciation and bioavailability to methylating bacteria in sediment pore waters. *Environ. Sci. Technol.* **33**, 951–957 (1999).
6. Zhang, T. et al. Methylation of mercury by bacteria exposed to dissolved, nanoparticulate, and microparticulate mercuric sulfides. *Environ. Sci. Technol.* **46**, 6950–6958 (2012).
7. Jonsson, S. et al. Mercury methylation rates for geochemically relevant Hg^{II} species in sediments. *Environ. Sci. Technol.* **46**, 11653–11659 (2012).
8. Zhang, T., Kucharzyk, K. H., Kim, B., Deshusses, M. A. & Hsu-Kim, H. Net methylation of mercury in estuarine sediment microcosms amended with dissolved, nanoparticulate, and microparticulate mercuric sulfides. *Environ. Sci. Technol.* **48**, 9133–9141 (2014).
9. Mazrui, N. M., Jonsson, S., Thota, S., Zhao, J. & Mason, R. P. Enhanced availability of mercury bound to dissolved organic matter for methylation in marine sediments. *Geochim. Cosmochim. Acta* **194**, 153–162 (2016).
10. Zhang, L. J. et al. Mercury sorption and desorption on organo-mineral particulates as a source for microbial methylation. *Environ. Sci. Technol.* **53**, 2426–2433 (2019).
11. Barnett, M. O. et al. Formation of mercuric sulfide in soil. *Environ. Sci. Technol.* **31**, 3037–3043 (1997).
12. Patty, C. et al. Using X-ray microscopy and Hg L_3 XAMES to study Hg binding in the rhizosphere of *Spartina* cordgrass. *Environ. Sci. Technol.* **43**, 7397–7402 (2009).
13. Gilmour, C. et al. Distribution and biogeochemical controls on net methylmercury production in Penobscot River marshes and sediment. *Sci. Total Environ.* **640**, 555–569 (2018).
14. Stordal, M. C., Gill, G. A., Wen, L. S. & Santschi, P. H. Mercury phase speciation in the surface waters of three Texas estuaries: importance of colloidal forms. *Limnol. Oceanogr.* **41**, 52–61 (1996).
15. Guentzel, J. L., Powell, R. T., Landing, W. M. & Mason, R. P. Mercury associated with colloidal material in an estuarine and an open-ocean environment. *Mar. Chem.* **55**, 177–188 (1996).
16. Deonarine, A. & Hsu-Kim, H. Precipitation of mercuric sulfide nanoparticles in NOM-containing water: implications for the natural environment. *Environ. Sci. Technol.* **43**, 2368–2373 (2009).
17. Poulin, B. A. et al. Effects of sulfide concentration and dissolved organic matter characteristics on the structure of nanocolloidal metacinnabar. *Environ. Sci. Technol.* **51**, 13133–13142 (2017).
18. Mazrui, N. M. et al. The precipitation, growth and stability of mercury sulfide nanoparticles formed in the presence of marine dissolved organic matter. *Environ. Sci. Proc. Impacts* **20**, 642–656 (2018).
19. Manceau, A., Wang, J., Rovezzi, M., Glatzel, P. & Feng, X. Biogenesis of mercury–sulfur nanoparticles in plant leaves from atmospheric gaseous mercury. *Environ. Sci. Technol.* **52**, 3935–3948 (2018).
20. Manceau, A. et al. Formation of mercury sulfide from Hg(II)–thiolate complexes in natural organic matter. *Environ. Sci. Technol.* **49**, 9787–9796 (2015).
21. Luo, H. W. et al. Photochemical reactions between mercury (Hg) and dissolved organic matter decrease Hg bioavailability and methylation. *Environ. Pollut.* **220**, 1359–1365 (2017).
22. Thomas, S. A., Rodby, K. E., Roth, E. W., Wu, J. S. & Gaillard, J. F. Spectroscopic and microscopic evidence of biomediated HgS species formation from Hg(II)–cysteine complexes: implications for Hg(II) bioavailability. *Environ. Sci. Technol.* **52**, 10030–10039 (2018).
23. Hochella, M. F. et al. Nanominerals, mineral nanoparticles, and earth systems. *Science* **319**, 1631–1635 (2008).
24. Wang, Y. F. Nanogeochemistry: nanostructures, emergent properties and their control on geochemical reactions and mass transfers. *Chem. Geol.* **378**, 1–23 (2014).
25. Sharma, V. K., Filip, J., Zboril, R. & Varma, R. S. Natural inorganic nanoparticles—formation, fate, and toxicity in the environment. *Chem. Soc. Rev.* **44**, 8410–8423 (2015).
26. Hochella, M. F. et al. Natural, incidental, and engineered nanomaterials and their impacts on the earth system. *Science* **363**, 1414–1424 (2019).
27. Lowry, G. V., Shaw, S., Kim, C. S., Rytuba, J. J. & Brown, G. E. Macroscopic and microscopic observations of particle-facilitated mercury transport from

New Idria and sulphur bank mercury mine tailings. *Environ. Sci. Technol.* **38**, 5101–5111 (2004).
28. Gilmour, C. C. et al. Sulfate-reducing bacterium *Desulfovibrio desulfuricans* ND132 as a model for understanding bacterial mercury methylation. *Appl. Environ. Microbiol.* **77**, 3938–3951 (2011).
29. Liu, L. et al. Facet energy and reactivity versus cytotoxicity: the surprising behavior of CdS nanorods. *Nano Lett.* **16**, 688–694 (2016).
30. Jun, Y. W. et al. Surfactant-assisted elimination of a high energy facet as a means of controlling the shapes of TiO_2 nanocrystals. *J. Am. Chem. Soc.* **125**, 15981–15985 (2003).
31. Graham, A. M., Aiken, G. R. & Gilmour, C. C. Effect of dissolved organic matter source and character on microbial Hg methylation in Hg-S-DOM solutions. *Environ. Sci. Technol.* **47**, 5746–5754 (2013).
32. Bouchet, S. et al. Linking microbial activities and low-molecular-weight thiols to Hg methylation in biofilms and periphyton from high-altitude tropical lakes in the Bolivian Altiplano. *Environ. Sci. Technol.* **52**, 9758–9767 (2018).
33. Rivera, N. A., Bippus, P. M. & Hsu-Kim, H. Relative reactivity and bioavailability of mercury sorbed to or coprecipitated with aged iron sulfides. *Environ. Sci. Technol.* **53**, 7391–7399 (2019).
34. Lower, S. K., Hochella, M. F. & Beveridge, T. J. Bacterial recognition of mineral surfaces: nanoscale interactions between *Shewanella* and α-FeOOH. *Science* **292**, 1360–1363 (2001).
35. Pedrero, Z. et al. Transformation, localization, and biomolecular binding of Hg species at subcellular level in methylating and nonmethylating sulfate-reducing bacteria. *Environ. Sci. Technol.* **46**, 11744–11751 (2012).
36. Dunham-Cheatham, S., Mishra, B., Myneni, S. & Fein, J. B. The effect of natural organic matter on the adsorption of mercury to bacterial cells. *Geochim. Cosmochim. Acta* **150**, 1–10 (2015).
37. Zhao, L. D. et al. Contrasting effects of dissolved organic matter on mercury methylation by *Geobacter sulfurreducens* PCA and *Desulfovibrio desulfuricans* ND132. *Environ. Sci. Technol.* **51**, 10468–10475 (2017).
38. Schaefer, J. K., Szczuka, A. & Morel, F. M. M. Effect of divalent metals on Hg(II) uptake and methylation by bacteria. *Environ. Sci. Technol.* **48**, 3007–3013 (2014).
39. Qian, C. et al. Quantitative proteomic analysis of biological processes and responses of the bacterium *Desulfovibrio desulfuricans* ND132 upon deletion of its mercury methylation genes. *Proteomics* **18**, 1700479 (2018).
40. Schaefer, J. K. et al. Active transport, substrate specificity, and methylation of Hg(II) in anaerobic bacteria. *Proc. Natl Acad. Sci. USA* **108**, 8714–8719 (2011).
41. Thomas, S. A., Mishra, B. & Myneni, S. C. B. Cellular mercury coordination environment, and not cell surface ligands, influence bacterial methylmercury production. *Environ. Sci. Technol.* **54**, 3960–3968 (2020).
42. Lin, H., Morrell-Falvey, J. L., Rao, B., Liang, L. & Gu, B. Coupled mercury–cell sorption, reduction, and oxidation on methylmercury production by *Geobacter sulfurreducens* PCA. *Environ. Sci. Technol.* **48**, 11969–11976 (2014).
43. Lu, X. et al. Nanomolar copper enhances mercury methylation by *Desulfovibrio desulfuricans* ND132. *Environ. Sci. Technol. Lett.* **5**, 372–376 (2018).
44. Brown, S. D. et al. Genome sequence of the mercury-methylating strain *Desulfovibrio desulfuricans* ND132. *J. Bacteriol.* **193**, 2078–2079 (2011).
45. Strehlau, J. H., Stemig, M. S., Penn, R. L. & Arnold, W. A. Facet-dependent oxidative goethite growth as a function of aqueous solution conditions. *Environ. Sci. Technol.* **50**, 10406–10412 (2016).
46. Guo, S. W., Ward, M. D. & Wesson, J. A. Direct visualization of calcium oxalate monohydrate crystallization and dissolution with atomic force microscopy and the role of polymeric additives. *Langmuir* **18**, 4284–4291 (2002).
47. Qiu, S. R. et al. Molecular modulation of calcium oxalate crystallization by osteopontin and citrate. *Proc. Natl Acad. Sci USA* **101**, 1811–1815 (2004).
48. De Yoreo, J. J. & Dove, P. M. Shaping crystals with biomolecules. *Science* **306**, 1301–1302 (2004).
49. Hsu-Kim, H. et al. Challenges and opportunities for managing aquatic mercury pollution in altered landscapes. *Ambio* **47**, 141–169 (2018).
50. Obrist, D. et al. A review of global environmental mercury processes in response to human and natural perturbations: changes of emissions, climate, and land use. *Ambio* **47**, 116–140 (2018).
51. Schaefer, K. et al. Potential impacts of mercury released from thawing permafrost. *Nat. Commun.* **11**, 4650 (2020).
52. Hintelmann, H. et al. Reactivity and mobility of new and old mercury deposition in a boreal forest ecosystem during the first year of the METAALICUS study. *Environ. Sci. Technol.* **36**, 5034–5040 (2002).
53. Meng, B. et al. The process of methylmercury accumulation in rice (*Oryza sativa* L.). *Environ. Sci. Technol.* **45**, 2711–2717 (2011).
54. Flemming, H.-C. & Wuertz, S. Bacteria and archaea on Earth and their abundance in biofilms. *Nat. Rev. Microbiol.* **17**, 247–260 (2019).
55. Brewer, T. E. & Fierer, N. Tales from the tomb: the microbial ecology of exposed rock surfaces. *Environ. Microbiol.* **20**, 958–970 (2018).
56. Russell, M. J. & Hall, A. J. The emergence of life from iron monosulphide bubbles at a submarine hydrothermal redox and pH front. *J. Geol. Soc. Lond.* **154**, 377–402 (1997).
57. Lovley, D. R. Dissimilatory Fe(III) and Mn(IV) reduction. *Microbiol. Rev.* **55**, 259–287 (1991).
58. Nealson, K. H. & Saffarini, D. Iron and manganese in anaerobic respiration: environmental significance, physiology, and regulation. *Annu. Rev. Microbiol.* **48**, 311–343 (1994).
59. Falkowski, P. G., Fenchel, T. & Delong, E. F. The microbial engines that drive Earth's biogeochemical cycles. *Science* **320**, 1034–1039 (2008).
60. Birks, L. S., & Friedman, H. Particle size determination from X-ray line broadening. *J. Appl. Phys.* **17**, 687–691 (1946).

Methods

Precipitation of HgS in the presence of natural ligands. The inorganic mercury stock solution consisted of $Hg(NO_3)_2$ (Sinopharm) dissolved in 0.02 M trace-metal-grade HNO_3. Na_2S stocks were prepared by dissolving freshly washed and dried crystals of $Na_2S{\cdot}9H_2O$ (Aladdin) in N_2-purged nanopure water (>18 MΩ cm), and were utilized within 4 h of preparation. Standard materials of NOM, including SRHA (catalogue no. 3S101H) and SRFA (catalogue no. 2S101F), were purchased from International Humic Substances Society (IHSS). NOM stock solution was prepared by dissolving NOM powder in nanopure water with pH adjusted to 7.5 using 0.01 M NaOH. The NOM stock solution was kept refrigerated, and filtered through 0.2-µm syringe filters, and the filtrate was analysed using combustion catalytic oxidation/infra-red spectroscopy (Multi N/C 3100 TOC, Analytik Jena AG). The powder stock of LMW thiol ligand, GSH (Aladdin), was kept refrigerated prior to dissolving in N_2-purged nanopure water. Stock solution of GSH was freshly prepared for each precipitation experiment and discarded after use.

The buffer solution for precipitation experiments contained 0.01 M $NaNO_3$ and 4 mM sodium 4-(2-hydroxyethyl) piperazine-1-ethanesulfonate (HEPES) with pH adjusted to 7.2 and then double-filtered to <0.05 µm. In this buffer solution, 50 µM $Hg(NO_3)_2$ and 50 µM Na_2S were mixed with 10 mgC L^{-1} SRHA or SRFA; 60 µM $Hg(NO_3)_2$ and 60 µM Na_2S were mixed with 100 µM GSH. The precipitation products were collected after ageing periods of 1, 11 and 21 days (in the dark, at room temperature, 23–26 °C), respectively, and utilized for material characterization and microbial methylation experiments. Precipitation experiments of $Hg(NO_3)_2$ and Na_2S in the same buffer solution without natural ligands were also conducted, and the precipitation products were included in the ageing experiments as control samples.

Preparation of model HgS nanoparticles. Model HgS nanoparticles with different exposed facets were synthesized using a sonochemical method[61]. For synthesizing model material I, 1.6 g $Hg(CH_3COO)_2{\cdot}2H_2O$ and 0.5 g thiourea (Aladdin) were mixed in 100 mL nanopure water, and the pH was adjusted to 4.0 using acetic acid. Then, 0.5 g polyvinylpyrrolidone (PVP, Mw 40 kD, Amresco) was added to the suspension, which was sonicated for 30 min while purged with nitrogen. The black-coloured precipitates were collected from the suspension using centrifugation, then thoroughly washed with absolute ethanol and nanopure water. Finally, the precipitates were heated at 300 °C for 2 h in the pipe furnace to remove the residual PVP. The procedure for preparing model material II was the same as that of model material I, except that no PVP was added to the experimental suspension. After synthesis, the total carbon content in the model materials was measured by using a TOC analyser (Multi N/C 3100 TOC, Analytik Jena AG), which gave values of 2.6% and 2.8% of the total particle mass for model material I and II, respectively, indicating minimal residual PVP on model material I. The two model materials were freeze-dried and stored in an anaerobic chamber with desiccants prior to material characterization and microbial methylation experiments.

Characterization of HgS nanoparticles. The particle morphology of the products of HgS precipitation experiments and the synthesized model nanoparticles was analysed using TEM-EDX (JEM-2100, JEOL). Samples for TEM analysis were prepared by depositing droplets of the particle suspensions on 200-mesh carbon-coated copper grids, and allowing the grids to air dry in an anaerobic chamber. For each type of HgS nanoparticle, the geometric diameters were obtained by measuring 100 particles from TEM images using ImageJ image processing software, based on which the geometric surface areas were calculated by assuming spherical particles with a density of 7.71 g cm^{-3} (refs. [6,62]). The crystallographic structures of the HgS nanoparticles were analysed by XRD spectroscopy on a diffractometer (Ultima IV, Rigaku Inc.) with Cu K_α radiation ($\lambda = 1.5418$ Å). The crystallite diameters were calculated using the Scherrer formula[60] from XRD data. HR-TEM was utilized to assess the lattice spacing of the crystalline nanoparticles to further corroborate the crystalline phases determined by XRD analysis. The surface elemental composition of HgS nanoparticles was characterized by XPS (Axis Ultra DLD, Kratos). The hydrodynamic diameters and zeta potential of nanoparticle aggregates were analysed by using a Zetasizer (Nano Series ZS90, Malvern).

Microbial methylation experiments. Methylating bacterium *D. desulfuricans* ND132 was cultured in Hungate tubes (Changshu Wente experimental ware co. LTD), which were kept in the dark at room temperature (23–26 °C) in an anaerobic chamber. The bacterial cultures were grown in sulfate-containing media and then transferred in fermentative media twice before mercury methylation experiments. The sulfate-containing media and fermentative media contain redox-sensitive resazurin as well as reductant Ti-nitrilotriacetic acid (NTA) to help maintain anaerobic conditions[28,63]. The inoculation ratio for the test cultures was 1:37 and 1:30 in the methylation experiments examining the bioavailability of the aged HgS precipitation products and the model nanoparticles, respectively.

Prior to addition of HgS nanoparticles, *D. desulfuricans* ND132 was pre-cultured to reach late-log growth phase. Stock suspensions of model materials I and II were prepared by adding the corresponding powder products into nanopure water, then sonicating for 120 min in anaerobic vials before taking aliquots. The total mercury addition for the methylation experiments of model nanoparticles and precipitation products was 50 nM and 10 nM, respectively. The pH of the test cultures was maintained at 7.0–7.3 using 3-(*N*-morpholino) propanesulfonic acid (MOPS). The test cultures were placed in the dark at room temperature (23–26 °C) in an anaerobic chamber during the entire time course of the methylation experiments. Two sets of controls were incubated under the same conditions, including (1) uninoculated media spiked with $Hg(NO_3)_2$ and (2) bacterial cultures without mercury addition. MeHg production in all control samples was below the detection limit (≤0.09 pM MeHg), thus abiotic methylation and mercury contamination were negligible in our experiments. At each time point, triplicate vials were collected and aliquots were taken for quantification of cell numbers using flow cytometry (Accuri C6 Plus, BD) after the bacterial cells had been stained with SYBR Green I (Life Technologies). Total mercury concentrations were measured using cold vapour atomic fluorescence spectrometry (CVAFS, Tekran 2600, Tekran)[64]. Afterwards, the rest of the cultures were preserved by 0.4% (v/v) trace-metal-grade HCl and kept refrigerated before MeHg analysis. MeHg concentrations were quantified by distillation, aqueous phase ethylation, gas chromatographic separation and CVAFS (Tekran 2700, Tekran)[65].

Mercury methylation bioassays were also carried out in the presence of divalent zinc, Zn(II). Zn(II) stock solutions were prepared by dissolving trace-metal-grade $ZnCl_2$ (Acros Organics) in 0.01 M trace-metal-grade HCl using degassed nanopure water. Zn(II) was injected into cultures of *D. desulfuricans* ND132 to reach final concentrations of 100–500 µM, before exposure to 10 nM HgS nanoparticles co-precipitated with GSH and aged for 1 day. The rest of the protocols were consistent with the other mercury methylation experiments conducted in this research.

Characterization of nanoparticle–bacteria association. In a subset of test cultures exposed to model materials I and II, bacterial cells with cell-bound nanoparticles were separated from unassociated nanoparticles by a density gradient centrifugation method using OptiPrep kit (Alere Technologies)[66]. Briefly, bacterial cells with bound and unbound nanoparticles were harvested by centrifugation at 9,000 rpm for 5 min. The pellets were resuspended in 1.5 mL 50% (w/v) OptiPrep medium and then centrifuged at 9,000 rpm for 5 min. Afterward, the top fraction (0.7 mL total) was used for quantification of cell-bound mercury, which was normalized with the cell numbers measured before centrifugation. The cell recovery during this procedure was assessed by measuring the protein content before and after gradient centrifugation using the bicinchoninic acid assay[67], and was found to be 93.9 ± 6.4%.

In a subset of test cultures exposed to HgS nanoparticles co-precipitated with SRHA, SRFA or GSH, samples were collected for TEM analysis by centrifugation. The pellets were washed with 10 mM phosphate buffered saline (PBS, pH 7.4), resuspended in fixative solution containing 2.5% (v/v) glutaraldehyde and stored at 4 °C overnight. The cells were washed with PBS again before and after being fixed in 1% (w/v) osmium tetroxide. Then, the samples were dehydrated with 30–100% (v/v) ethanol, embedded in Epon812 epoxy resin and cured at 37 °C, 45 °C and 65 °C for 24 h, respectively. Subsequently, they were sliced into ultra-thin sections by using an UltracutE microtome. These sections were deposited on 200-mesh carbon-coated copper grids and analysed by TEM (JEM-1200EX, JEOL) and EDX (OXFOR MAX80, Oxford Instruments).

MD simulations. The protein sequence and three-dimensional structure of periplasmic solute-binding protein of zinc transport system of *D. desulfuricans* ND132, ZnuA, was obtained from the UniProt database (https://www.uniprot.org/uniprot/F0JJA9) and predicted by ITASSER online service[68–70]. The crystal structure of metacinnabar was taken from the Materials Project website (https://materialsproject.org/materials/mp-1123/). The spherical structures of facet (111), (220) and (311) were constructed by the software module of BIOVIA Materials Studio 2017. All of the MD calculations were carried out using the GROMACS 5.0.4 package[71–73] in the *NPT* ensemble. The protein force field was implemented using the Amber 99SB-ILDN all-atoms force field[74]. The parameters of the facets were taken from literature[75] and generated by the x2top command in GROMACS.

MD simulation was performed from 0 to 100 ns for each calculation. The temperature was stabilized at 298 K by Nosé–Hoover thermostat coupling[76]. The cut-off switching function for calculating the non-bonded van der Waals interactions started at 1.2 nm and reached zero at 1.35 nm. The long-range electrostatic interaction was calculated by particle mesh Ewald[77] summation with a truncation radius of 1.2 nm. Periodic boundary conditions were used throughout the calculation. The limitation of bond length was implemented through the linear constraint solver algorithm[78]. The hydrated layers were modelled as point-charge water molecules[79]. The system was kept neutral by adding chloride and sodium ions. The time step of calculated data was 2 fs. Molecular graphics and visualization were performed using the free VMD software[80].

Adsorption of natural ligands to model nanoparticles. Adsorption experiments were performed in a series of 40-mL EPA vials containing 0.01 M $NaNO_3$. SRHA, SRFA or GSH with an initial concentration of 10 mgC L^{-1}, 10 mgC L^{-1} or 100 mg L^{-1} was added to vials containing 1,000 mg L^{-1} model materials I or II, respectively.

For all the adsorption experiments, the pH of the reaction matrix was adjusted to 7.0 ± 0.7 using HNO_3 and NaOH. The vials were then kept at room temperature (23–26 °C) on a rotating mixer at a speed of 70 rpm. Two sets of controls were incubated under the same conditions: (1) HgS nanoparticles with no ligands and (2) SRHA, SRFA or GSH with no nanoparticles. At each time point, triplicate vials were sacrificed and centrifuged at 12,000 rpm for 3 min, which effectively separated the adsorbed ligands from free ligands according to the controls (that is, <2% HgS nanoparticles and >99% ligands remained in the supernatant after centrifugation). The supernatant was sampled to determine the concentration of unadsorbed SRHA, SRFA or GSH, and the amount of adsorbed ligand was calculated using a mass balance approach. The concentrations of SRHA and SRFA were measured by using a TOC analyser (Multi N/C 3100 TOC, Analytik Jena AG), and the GSH concentration was quantified with a total amino acid assay kit (Nanjing Jiancheng Bioengineering Institute).

DFT calculations. The adsorption of GSH on the (111), (220) and (311) facets of metacinnabar was simulated using DFT analysis conducted with the Vienna Ab-Initio Simulation Package (VASP). The electron–ion interaction was assessed by the projector-augmented wave method, and the cut-off value of the plane wave was 420 eV. The Perdew–Burke–Ernzerhof (PBE)[81–83] method was used to describe the exchange and correlation potential, with spin polarization considered in all computations. The electronic structure calculations were carried out with Gaussian smearing of 0.1 eV, and $1 \times 1 \times 1$ Monkhorst–Pack **k**-point grids were used to sample the Brillouin zone[84].

We used a (3×3) repeated unit cell with a four-layer slab for the (111), (220) and (311) surfaces for GSH adsorption. All slabs were spaced by more than 14 Å perpendicular to the slab surface to avoid artificial interaction due to periodicity. During optimization, the atoms of the two layers at the bottom were fixed, and the remaining atoms were relaxed to reach stable configurations. Atoms were optimized until the residual forces were below 0.02 eV $Å^{-1}$. The adsorption energies were estimated using the equation

$$E_{ads}A = E_{slab+A} - E_{slab} - E_A \quad (1)$$

where $E_{ads}A$ is the interaction energy between the slab fragment and molecule fragment in the optimized configurations, E_{slab+A} is the total energy of the slab and the molecule in the optimized configurations, E_{slab} is the energy of the slab alone in the optimized configurations and E_A is the energy of the molecule alone in the optimized configurations.

Statistical analyses. Statistical differences were analysed by one-way analysis of variance (ANOVA) for comparisons of three test groups, and by the two-tailed independent *t* test for comparisons of two test groups, using Statistical Product and Service Solutions (SPSS) software version 19.0. *P* values less than 0.05 ($P < 0.05$) were considered statistically significant.

Data availability

The protein sequence and three-dimensional structure of periplasmic solute-binding protein of zinc transport system of *D. desulfuricans* ND132, ZnuA, are available in the UniProt database (https://www.uniprot.org/uniprot/F0JJA9). All source data are deposited in the Open Science Framework (OSF) at https://doi.org/10.17605/OSF.IO/YXRMF. Source Data files and a Supplementary Data file are provided with this paper.

References

61. Wang, H. & Zhu, J. J. A sonochemical method for the selective synthesis of α-HgS and β-HgS nanoparticles. *Ultrason. Sonochem.* **11**, 293–300 (2004).
62. Chichagov, A. V. *Crystallographic and Crystallochemical Database for Minerals and Their Structural Analogues* (Institute of Experimental Mineralogy, Russian Academy of Science, 2020); http://database.iem.ac.ru/mincryst/index.php
63. Benoit, J. M., Gilmour, C. C. & Mason, R. P. Aspects of bioavailability of mercury for methylation in pure cultures of *Desulfobulbus propionicus* (1pr3). *Appl. Environ. Microbiol.* **67**, 51–58 (2001).
64. *Method 1631, Revision D: Mercury in Water by Oxidation, Purge and Trap, and Cold Vapor Atomic Fluorescence Spectroscopy* (US EPA, 2001).
65. *Method 1630: Methyl Mercury in Water by Distillation, Aqueous Ethylation, Purge and Trap, and CVAFS* (US EPA, 2001).
66. Mortimer, M., Petersen, E. J., Buchholz, B. A., Orias, E. & Holden, P. A. Bioaccumulation of multiwall carbon nanotubes in tetrahymena thermophila by direct feeding or trophic transfer. *Environ. Sci. Technol.* **50**, 8876–8885 (2016).
67. Smith, P. K. et al. Measurement of protein using bicinchoninic acid. *Anal. Biochem.* **150**, 76–85 (1985).
68. Roy, A., Kucukural, A. & Zhang, Y. I-TASSER: a unified platform for automated protein structure and function prediction. *Nat. Protoc.* **5**, 725–738 (2010).
69. Yang, J. et al. The I-TASSER suite: protein structure and function prediction. *Nat. Methods* **12**, 7–8 (2015).
70. Yang, J. & Zhang, Y. I-TASSER server: new development for protein structure and function predictions. *Nucleic Acids Res.* **43**, W174–W181 (2015).
71. Abraham, M. J. et al. GROMACS: high performance molecular simulations through multi-level parallelism from laptops to supercomputers. *SoftwareX* **1-2**, 19–25 (2015).
72. Pronk, S. et al. GROMACS 4.5: a high-throughput and highly parallel open source molecular simulation toolkit. *Bioinformatics* **29**, 845–854 (2013).
73. Van der Spoel, D. et al. GROMACS: fast, flexible, and free. *J. Comput. Chem.* **26**, 1701–1718 (2005).
74. Lindorff-Larsen, K. et al. Improved side-chain torsion potentials for the Amber ff99SB protein force field. *Proteins* **78**, 1950–1958 (2010).
75. Fuchs, J. F. et al. New model potentials for sulfur–copper(I) and sulfur–mercury(II) interactions in proteins: from ab initio to molecular dynamics. *J. Comput. Chem.* **27**, 837–856 (2006).
76. Evans, D. J. & Holian, B. L. The Nose–Hoover thermostat. *J. Chem. Phys.* **83**, 4069–4074 (1985).
77. Tom, D., Darrin, Y. & Lee, P. Particle mesh Ewald: an *N*·log(*N*) method for Ewald sums in large systems. *J. Chem. Phys.* **98**, 10089–10092 (1993).
78. Hess, B., Bekker, H., Berendsen, H. J. C. & Fraaije, J. G. E. M. LINCS: a linear constraint solver for molecular simulations. *J. Comput. Chem.* **18**, 1463–1472 (1997).
79. Jorgensen, W. L., Chandrasekhar, J., Madura, J. D., Impey, R. W. & Klein, M. L. Comparison of simple potential functions for simulating liquid water. *J. Chem. Phys.* **79**, 926–935 (1983).
80. Humphrey, W., Dalke, A. & Schulten, K. VMD: visual molecular dynamics. *J. Mol. Graph.* **14**, 33–38 (1996).
81. Kresse, G. & Hafner, J. Ab initio molecular dynamics for liquid metals. *Phys. Rev. B* **48**, 13115–13118 (1993).
82. Kresse, G. & Furthmüller, J. Efficient iterative schemes for ab initio total-energy calculations using a plane-wave basis set. *Phys. Rev. B* **54**, 11169–11186 (1996).
83. Kresse, G. & Joubert, D. From ultrasoft pseudopotentials to the projector augmented-wave method. *Phys. Rev. B* **59**, 1758–1775 (1999).
84. Monkhorst, H. J. & Pack, J. D. Special points for Brillouin-zone integrations. *Phys. Rev. B* **13**, 5188–5192 (1976).

Acknowledgements

This research was supported by the National Key Research and Development Program of China under grant 2018YFC1800705 (to T.Z.), the National Natural Science Foundation of China under grants 22020102004 (to W.C.), 21976095 (to T.Z.) and 41603099 (to T.Z.), and the Ministry of Education of China under grant T2017002 (to W.C.). Partial support for P.A. was provided by the NSF Nanosystems Engineering Research Center for Nanotechnology-Enabled Water Treatment (ERC-1449500). The authors thank C. C. Gilmour from the Smithsonian Environmental Research Center for supplying the strain of *D. desulfuricans* ND132, Q. Yao for help with XRD analysis and H. Hsu-Kim and H. H. Teng for helpful discussions regarding manuscript preparation.

Author contributions

L.T., W.G., Y.J. and X.H. carried out the experiments and data analysis. T.Z. conceived the study and supervised the research. W.C. and P.J.J.A. contributed intellectual input to the experimental design and data analysis. L.T. and T.Z. drafted the manuscript with input from all authors.

Competing interests

The authors declare no competing financial interests.

Additional information

Supplementary information The online version contains supplementary material available at https://doi.org/10.1038/s41561-021-00735-y.

Correspondence and requests for materials should be addressed to T.Z.

Peer review information *Nature Geoscience* thanks José Pérez-Donoso and the other, anonymous, reviewer(s) for their contribution to the peer review of this work. Primary Handling Editors: Clare Davis; Rebecca Neely.

Reprints and permissions information is available at www.nature.com/reprints.